Chapter - 2

Thin Film Deposition and Characterization Techniques

2.1 INTRODUCTION

This chapter discusses, various instrumental details, which have been used for the experimental works related to the thesis. Vacuum assisted thermal evaporation and RF/DC Sputter deposition units have been used for the preparation of thin metal films as well as oxide layers. Thermal oxidation of as grown metal films has been carried out in air as well as in controlled O_2 ambient or in the presence of inert gasses for the preparation of oxides thin films. The growth mechanism of oxides thin films is affected by various parameters such as thickness, oxygen partial pressure, annealing temperature and duration, etc.

The experimental characterization carried out include X-ray diffraction (XRD), scanning electron microscope (SEM), four probe measurement, and X-ray photoelectron spectroscopy (XPS). The structural information such as crystal structure, oxide phase purity and crystallite size estimation of the oxide films have been examined by X-ray diffraction (XRD). Transmission electron microscopy (TEM) has also been used to gather structural information of the surface and its underneath. Scanning electron microscopy (SEM) and atomic force microscopy (AFM) provide the information about the surface morphology and topography of the oxide surface, respectively. Electronic transport properties of the oxide surface such as surface resistivity, carrier concentration, hall parameters have been measured using probe measurement techniques. The optical properties such as absorption, reflection, transmission have been measured to get the information about the band gap of the oxide materials, using UV-visible spectroscopy. In addition, Raman spectroscopy was also used for optical analysis of metal oxides phase purity. Finally, X-ray photoelectron spectroscopy (XPS) and Energy Dispersive X-ray (EDX) analysis have also been applied to get the information about the chemical composition and oxidation states of the metal oxides thin films. The related theory and working principal of these characterization techniques are briefly described here.

2.2 THIN FILM DEPOSITION TECHNIQUES

Controlled growth of a thin layer of materials on to the surface of any substrate starting from micron down to few nanometer scales is known as a thin film deposition. In thin film deposition process, two surfaces of same or different materials come very close to each other which can significantly influence their internal properties, making it very different from their bulk properties. Various techniques are used for the deposition of thin films, which can be classified into two broad categories such as *Physical Route* and *Chemical Route,* based on the nature of the deposition process involved [1]. Physical routes are mainly depending upon the evaporation and ejection of the target material from a source into gas phase under vacuum or controlled ambient, followed by its condensation on a desired substrate. Whereas, chemical routes involve various chemical precursors, their chemical reaction pathways, followed by proper filtrations leading to the desired material states. However, the possibility to control the unwanted contamination is relatively high in physical method as the number of processing steps is largely reduced in physical route. Therefore, our main focus would be to exploit different physical vapor deposition techniques (physical routes) to grow metal oxide thin films which are discussed in the following.

2.2.1 Physical Vapor Deposition

Physical Vapor Deposition (PVD) describes a variety of vacuum assisted deposition method, where materials are physically transferred from one place (crucible) to other (substrate) in a controlled (thickness) manner, without having any major chemical changes. PVD is characterized by a process in which the materials go from a solid phase to its vapor phase and then condensed back to solid state in the form of a thin film on desired substrate. The most common PVD processes are generally sputtering and thermal evaporation techniques which are discussed in the following. The major procedures involved in physical vapor deposition can be summarized as:

(I) Removal of source material from the crucible to gas phase at high temperature by thermal evaporation / reactive ion sputtering / laser sublimation.

(II) Collision free transportation of source material in gas phase from crucible to substrate under vacuum / low pressure.

(III) Condensation of source material from gas phase to substrate in a controlled manner at relatively lower temperature / room temperature.

2.2.1.1 Thermal evaporation technique

Thermal evaporation is a convenient and simplest method of PVD for the deposition of thin films. Generally, a solid material such as metal, alloy or compound is placed in an energetic source known as filament, crucible or boat. By passing a very high current (up to 200A) through the boat (a thin metal foil), source material (which is placed into the boat) become very hot and after reaching its melting point directly escaped to its vapor phase. The whole process is performed within a closed chamber under vacuum of ~ 10^{-6} mbar, where the particles are free to move without having any collision. Now these particles in vapor form tend to follow a straight path and condense on the substrate surface in the form of a thin film. To prevent any kind of contamination from the crucible material, the filaments are made up of inert material such as Tantalum (Ta), Molybdenum (Mo) or Tungsten (W), which are having high melting point, very low vapour pressure and chemical inert. Figure 2.1 show (a) schematic representation of the setup and (b) the actual image of our thermal evaporation deposition unit, respectively. A detailed study of the thermal evaporation technique has been discussed by *L. Holland* [2].

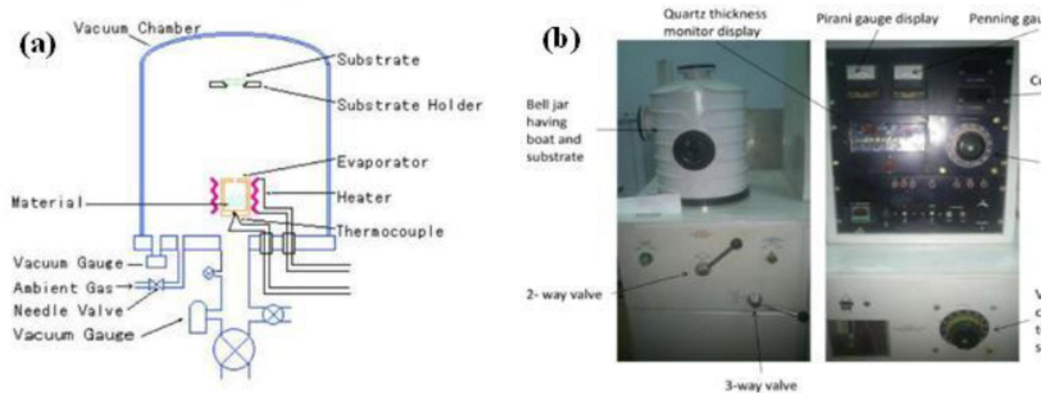

Figure 2.1: *(a) Schematic representation [3] and (b) actual view of thermal evaporation deposition unit.*

The uniformity and quality of any thin films is mainly affected by the evaporation / deposition rate, chamber pressure (r >>l), substrate rotation, substrate temperature etc. The thickness of the film is essentially depends upon two significant parameters such as:

(i) Deposition rate in the chamber pressure

(ii) Position of substrate with respect to filament

Relation between the chamber pressure (P) and mean free path (λ) are given below:

$$\lambda = \frac{5\times10^{-3}}{P(\text{torr})}(\text{cm}) \tag{2.1}$$

The mean free path (λ), *i.e.,* the average distance between two successive collisions of any gas molecule, is inversely proportional to the chamber pressure (P). If the chamber pressure is relatively high then mean free path is getting smaller, which would point towards a lot of collisions between the deposit vapour molecules before reaching to the substrate and hence the distance between the source and the substrate have to be considerably reduced to have a smooth film deposition. Therefore, to have a collision free transport of the deposit material from the source to the substrate, a lower chamber pressure (~10^{-6} torr) has to be maintained. The relation between film thicknesses (R) with the distance of the substrate to the source (r) at an evaporation temperature is reported as the "Langmuir Knudsen" relation [4] is depicted below. The mass deposition rate per unit area of source surface is

$$R_m = C_m\left(\frac{M}{T}\right)^{\frac{1}{2}}\cos\theta\cos\phi\frac{1}{r^2}\left(P_e(T)-P\right) \tag{2.2}$$

where, C_m is a constant and equal to 1.85×10^{-2}, r is source substrate distance, T is source temperature, P_e is evaporant vapor pressure (torr) as a function of T within the *Knudsen cell*, P is chamber pressure and M is molecular mass of evaporant. It is clear from "Langmuir Knudsen" relation that the deposition rate depends upon the position of as well as surface angle of the flat substrate [5]. However, it can be independent of the angle for a spherical substrate surface.

In present work, substrate with a flat surface is used during the thin film deposition process. According to "Langmuire Knudsen" relation the thickness variation of the films is mainly affected by the positions on the substrates. If consider that the deposition rate at the center of the substrate is R_1 and at the edge is R_2 on flat surface holder then the relation is given as [5]:

$$R_1\alpha\frac{1}{r_1^2}, R_2\alpha\frac{1}{r_2^2}\cos^2\theta = \frac{r_1^2}{r_2^4} \tag{2.3}$$

and the uniformity is defined as

$$\alpha(\%) = \frac{R_1 - R_2}{R_1}(\%) \tag{2.4}$$

However, the distance between the substrate and cell is assumed to be much larger here as compare to the substrate size. Therefore, a homogeneous film thickness is also expected for our study

2.2.1.2 DC/RF Magnetron sputtering

Sputtered deposition unit is non-thermal PVD method, where energetic ions are used to remove the deposit materials to form a thin film. Sputtering is the process of ejection of atoms from the target material surface by bombardment of energetic particle or by momentum transfer process between the sputter gas ions and target atoms. Mainly, two methods such as Radio Frequency (RF) sputtering and Direct Current (DC) sputtering are used. Further details related to sputtering unit for different materials are discussed by *K. Wasa & his group* in 2004 [4].

Usually, DC/RF magnetron sputtering system is capable to grow composite materials by co-sputtering technique [6]. Radio frequency (RF) magnetron sputtering system is used for growing non-magnetic thin films of all materials including both highly insulating and conducting materials, in a controlled way and the deposition rate can be controlled by adjusting power and working pressure. This system is also integrated with DC power supply to deposit only conducting materials (W, Ag, Ti, Cu and Zn) [7]. Schematic view and set-up image of sputter system with various components is shown in Figure 2.2. In this present work, a spherical sputter system having two sputters guns is used. These guns have either an *in-situ* tilt angles of (±15°) or arranged at 60° to each other at the bottom of the chamber. For metallic (Cu or Zn) targets, 18W of D.C. power supply was maintained for the DC sputtering. However, for semiconducting metal oxides (copper oxide and zinc oxide) deposition, RF power was varied from 30W to 80W in RF sputtering unit. Sputter targets of two-inch diameter was used for the deposition of thin films. In order to have a uniform deposition of thin films over the whole surface, substrate rotation (> 10rpm) facility was also used. The target material was connected to the negative terminal of power supply (cathode) whereas, the substrate holder along with the chamber were maintained at a ground potential (act as the anode). After vacuum formation, the

sputtering chamber is generally filled with inert gasses, typically argon (11.5 sccm), which was used as a sputtering gas at 1.8×10^{-2} mbar. The glow discharge plasma is created by applying a DC voltage between the electrodes. The Ar^{+} ions (generated in the glow discharge) are then accelerated towards the cathode and hits the surface of target materials with high energy which successfully sputters (removes) the target atom to gas phase. Initially, Ar^{+} ions are converted to neutral Ar atom by capturing the electrons on the surface of the target or the surrounding. Apart from the neutral Ar atoms, charged atoms and electrons are also emitted from the surface. These ejected atoms are then condensed on a substrate at an optimal distance from the target to form the thin film [Figure 2.2 (a)]. Many growth parameters can influence the deposition process such as chamber pressure, sputter gas pressure [10], sputter gun power and substrate temperature [11]. In addition, the relative orientation of target and substrate surfaces can also affect the film growth process.

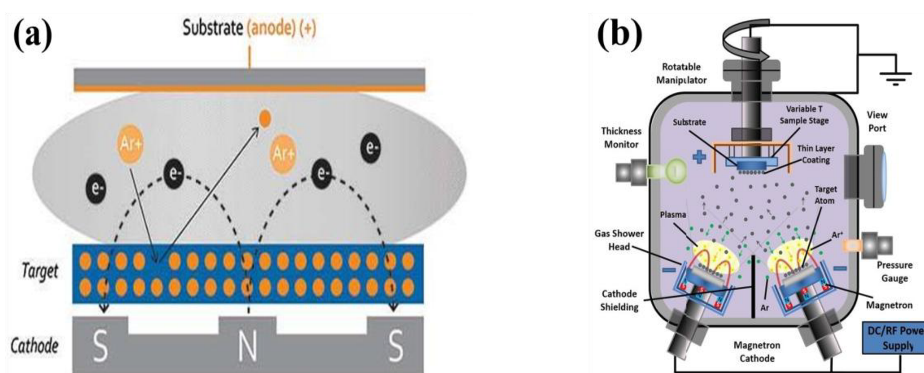

Figure 2.2: *(a) Schematic view of (a) plasma creation [8] and (b) DC/RF magnetron sputtering unit, of a sputter system [9].*

2.3 CHARACTERIZATION OF METAL OXIDE THIN FILMS

The major part of the experimental characterizations has been carried out using following analytical techniques such as four probe measurement techniques, X-ray diffraction (XRD), scanning electron microscope (SEM) and X-ray photoelectron spectroscopy (XPS), Raman spectroscopy, UV-Vis spectroscopy etc. The structural information such as crystal structure and phase purity of the oxide surface has been examined by X-ray diffraction (XRD). Transmission electron microscopy (TEM) has also been used to gather structural information of the surface topography of oxide thin

films. Scanning electron microscopy (SEM) and atomic force microscopy (AFM) give the information about the surface morphology and topography of the oxide surface, respectively. Electronic information about the oxide surface, like resistivity, hall parameters can be measured using probe method. The optical properties such as absorption, reflection, transmission have been measured to get the information about the band gap of oxide thin films, using UV-visible spectroscopy. In addition, Raman spectroscopy was also used for optical analysis of metal oxides thin films. Finally, X-ray photoelectron spectroscopy (XPS) and Energy Dispersive X-ray (EDX) analysis have also been applied to get the information about the surface chemical composition of metal oxides thin films. The related theory and working principal of these characterization techniques are briefly described here.

2.3.1 X-Ray Diffraction (XRD)

The discovery of X-rays makes it possible for the scientists to investigate the structure of a crystalline solid down to the atomic level. Typically, X-ray is an electromagnetic radiation having wave length of ~1Å which is used as a probe for the investigation of crystal structures, crystallite size, dislocation density and lattice strain of the target materials. X-ray diffraction peak profile of thin films is slightly different from their bulk and directly depends on the availability of the diffraction volume. The relative intensity peak does not show any variation with the JCPDS (Joint Committee on Powder Diffraction Standards) file for bulk samples whereas in case of thin films a small variation in relative peak intensity is observed with incident angle θ due to the asymmetric irradiating volume distribution. Generally, the powder X-ray diffractometer is designed to study the epitaxial thin films [shown in Figure 2.3(a)], which requires some important features such as alignment of the X-ray source and the detector. In addition, if the sample/target rotates by an angle θ, then the detector moves by an angle of 2θ. Some relevant fundamentals of the X-ray diffraction were discussed in 1974`s textbook, written by *Klug and Alexander* [12].

The basic principle of XRD is based on the diffraction phenomenon of electromagnetic wave. X-ray is generated in a cathode ray tube by heating a filament to produce the thermo-ionic electrons, which are then accelerated under vacuum toward a target, by applying a high voltage (KV) between them. These high-speed electrons are

interacting with the target material and lost their energy, as a result EM radiation emits in the form of X-ray. This X-ray is then directed towards the crystalline surface to make the diffraction process. If the scattered X-ray beam makes a constructive interference with the incident one, Bragg`s condition will satisfy and high intensity diffracted spots will be produced. Bragg's formula for X-ray diffraction, which is used to determine the crystal structure, is given below [13]:

$$2d_{hkl}\sin\theta = n\lambda \text{ and } \quad n = 0, 1, 2, 3\ldots\ldots \tag{2.5}$$

Where, d_{hkl} is the inter planer spacing between (h k l) crystal planes, θ is the grazing angle and λ is the wavelength of X-ray. Here, (hkl) represents the Miller indices and n denotes the order of diffraction.

Figure 2.3: *(a) Schematics view of rotating crystal X-ray diffraction method with θ-2θ scan, (b) sample mounting state and rotating detector set up and (c) closed chamber X-ray diffractometer.*

After calculating the value of d_{hkl} and determining the Miller indices (depending on the crystal structure), we can easily find the lattice parameter (a, b and c) of the crystalline solids. The relation between the lattice parameters (a, b and c), Miller indices (hkl) and the inter-planer distance (d) are given as [14]:

$$\frac{1}{d^2} = \frac{1}{\sin^2\beta}\left(\frac{h^2}{a^2} + \frac{k^2\sin^2\beta}{b^2} + \frac{l^2}{c^2} - \frac{2hl\cos\beta}{ac}\right) \tag{2.6}$$

Where, β is the full-width half maximum (FWHM) and it contributes to the peak broadening. As the average crystallite size decreases, the full width increases. The average crystallite size (D) of any thin film can be determined by using 'Debye Scherrer formula' as given below [15]:

$$D = \frac{k\lambda}{\beta\cos\theta} \tag{2.7}$$

Where, k is a constant known as shape factor. The origin of micro strain (ε) is also calculated using the relation [15]:

$$\varepsilon = \frac{\beta \cos\theta}{4} \tag{2.8}$$

The dislocation density (δ) is defined as the dislocation lines per unit area of the crystal, which can also be evaluated from the crystallite size 'D' using the formula [14]:

$$\delta = \frac{1}{D^2} \tag{2.9}$$

In the present work, metal oxide thin films were extensively been analyzed using the X-ray powder diffractometer from RIGAKU MiniFlex II [shown in Figure 2.3(b) and (c)], working at room temperature. A typical Cu K_α radiation (λ = 1.54 Å) is used as X-ray source and using an accelerating potential of 30kV and filament current of 30mA.

2.3.2 Field Emission Scanning Electron Microscope (FESEM)

The field emission Scanning Electron Microscopy (FESEM) is a technique, which uses a beam of electrons as probe to scan over a conducting surface to form images of the sample surface (morphology), with a very high special resolution of about 10 nm. When a focused beam of electrons is incident on the matter, only a small portion of the upper part (interaction volume) is interacted with the incident electron beams, and results in secondary electron emission. These secondary electrons are further used for the investigations which finally represent the surface morphology of the sample. It is to be noted that sample preparation for FESEM is quite simple and requires non-magnetic and conducting samples to avoid any charging effect. In case any non-conducting samples, usually a very thin gold (Ag) layer is sputtered on the surface of oxide thin films, prior to the imaging. Figure 2.4 (a) show a schematic drawing of the field emission scanning electron microscope (FESEM).

Basically, in SEM imaging, an electron gun emits highly energetic electrons beam which travel downward through a series of magnetic lenses and strikes to the surface of the sample. The beam is collimated by an electromagnetic condenser lens and focused to a very fine spot by an objective lens. Near the bottom area, a set of electromagnetic scanning coils move the focused beam back and onward across the specimen surface to scan over it. When the electron beam hits the sample, various kinds

of transitions such as backscattered electrons, secondary electrons, transmitted electron, auger electrons and X-ray photons are produced [shown in Figure 2.4 (b)]. The surface imaging of SEM is only obtained by secondary electrons, which are collected by secondary electron detector and converted in to an amplified voltage. The amplified voltage is applied to the grid of the CRT (Cathode Ray Tube), which causes the intensity modulation to image contrast. The image consists of thousands of spots of different intensities on a CRT, that finally relate to the morphology of the sample surface. Further details related to SEM were discussed by *R. F. Egerton* in 2005 [16].

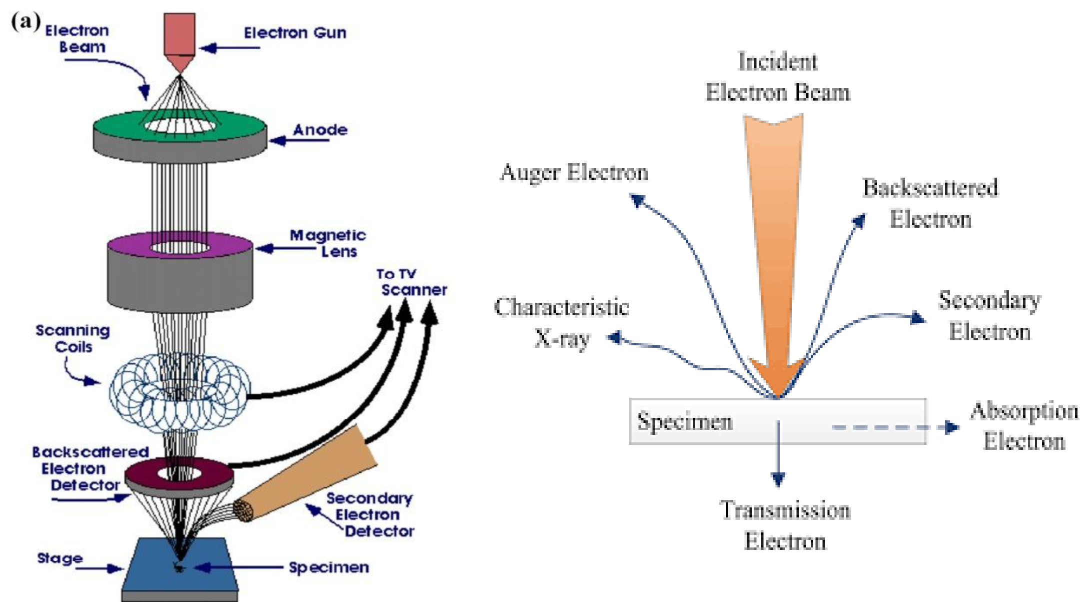

Figure 2.4: *Schematic drawing of (a) field emission scanning electron microscope (FESEM) [17] and (b) interaction of focused electron beam with the matter [18].*

2.3.3 Transmission Electron Microscope (TEM)

The Transmission Electron Microscope (TEM) is the first type of electron microscope, which has been developed by Max Knoll and Ernst Ruska in 1931. Transmission electron microscopy (TEM) is capable for imaging at higher resolution, due to the small 'de Broglie wavelength' of high energy electrons. It makes possible to examine the detailed studies of a single column of atoms. During the transmission process, electrons are interacting with matter and scattering process has take place. The elastically scattered electrons are keeping the constant energy but change the direction which is similar to the Rutherford scattering experiment, where α-particles were used. This scattering process is mainly dependent on the atomic mass of the

scattering material. Hence, a mass dependent contrast can be obtained after proper imaging of the transmitted electrons, which gives the information about the lattice imaging of different crystalline materials. For a crystalline sample, the scattering process can lead to the formation of diffraction patterns following the Bragg reflection of the electrons wave functions during transmission [19]. A schematic drawing and digital image of TEM is shown in Figure 2.5 (a) and (b), respectively.

In TEM, a parallel beam of highly monochromatic electron is directed towards the thin crystalline sample. The parallel beam of electron strikes to the sample volume and transmitted, which is used for the further TEM imaging. A schematic drawing and digital image of system of TEM is shown in Figure 2.5(a) and (b) respectively. The transmitted beam of electrons is focused using objective lens and selected area diffraction (SAD) apertures. Afterword two basic patterns, diffraction pattern [Figure 2.5(a) (I)] and the image formation [Figure 2.5(a) (II)] is produced [19]. The diffraction pattern or image is formed from the interaction of the electrons transmitted through the sample. The diffraction pattern is observed in the back focal plane of the objective lens, which represent the image of the reciprocal lattice space. The selected area aperture is virtually reduces the illuminated area of the sample, contributing to the diffraction and also able to examine the periodic diffraction of electrons from the lattice plane. Generally, the diffraction pattern contains the bright secular reflected beam at the center (00), which is selected for imaging and known as “bright spot” image. Whereas, higher order diffracted beam is also used for imaging for “dark spot” image. The selection of the diffraction spot can be obtained by moving the objective aperture or oriented the incident electron beam. The TEM image is finally focused onto a phosphorus image screen and light is generated to allow the user to see the image [19-20].

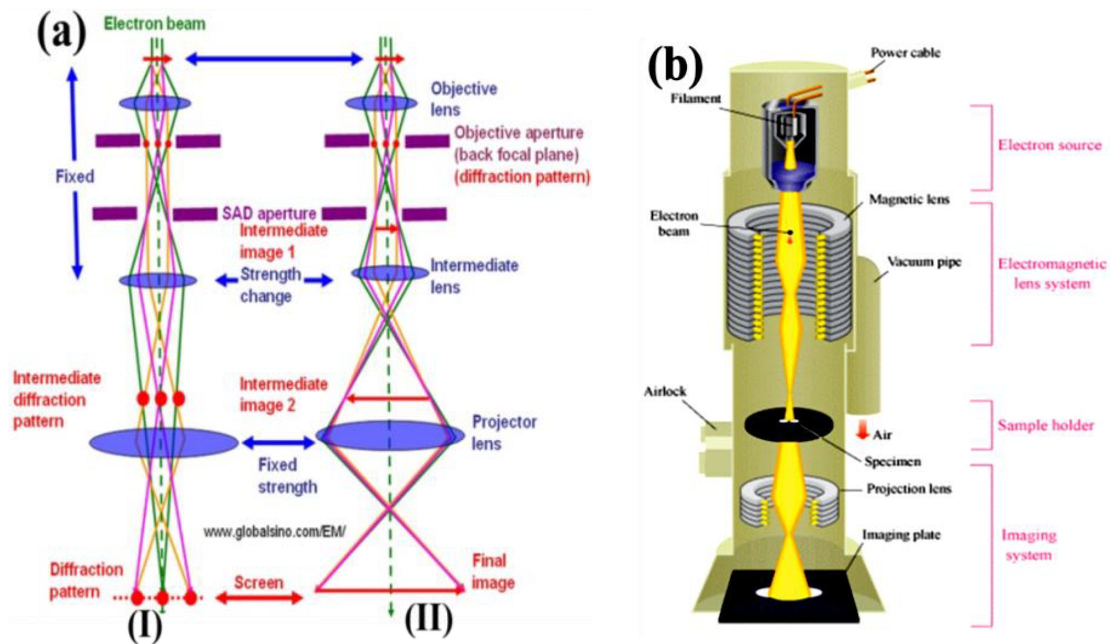

Figure 2.5: *(a) Two basic operations (I) diffraction patterns and (II) image formation [21] and (b) schematic view of the transmission electron microscopy [22].*

2.3.4 Scanning tunneling microscope (STM)

In 1981, two IBM scientists, Gerd Binnig and Heinrich Rohrer developed a new technique known as Scanning Tunnelling Microscopy (STM), for studying the surface atomic structure. The development of STM makes it possible to obtain the real space images of metal and semiconductor surfaces with an atomic resolution for the first time. It can also provide the information about the local electronic states of the surface o the samples down to the atomic scale. Moreover, it can also be operated in liquids [19, 23].

STM is a multipurpose instrument and mainly divided into two types: (i) microscopic imaging mode (known as topography) and (ii) spectroscopic mode. In addition, there are many other options such as spin polarized scanning tunnelling microscope (SPSTM), Ballistic electron emission microscope (BEEM), scanning field emission microscope (SFEM) [24]. Microscopic imaging mode is deals with the surface atomic structures of the samples, whereas, the spectroscopic mode is given the information about the electronic states of surface. Two data acquisition's options are possible in microscopic imaging mode of STM, which is mainly depending on the action of feedback loop. The tunnelling current remains constant during the action of feedback

loop and this type of imaging mode is known as constant current mode. If the feedback loop is turn off then the tip scans over the surface at a constant height and the imaging mode is known as constant height mode [19]. For a constant bias voltage, tunneling current not only depends upon the gap distance between the tip and surface atoms, but also on the barrier height of the tip surface junction. Similar to microscopic mode, two major types of spectroscopy modes are also available. (i) I-V spectroscopy mode: This mode provides the information about electronic properties of the surface such as the position of valance band (VB) and conduction band (CB). Variation in the tunnelling current with respect to the bias voltage is measured for a fixed tip-surface height. (ii) I-Z spectroscopy: This mode provides the information about the local barrier height of the surface, where the variation in tunnelling current with respect to the tunnelling gap is measured at a constant bias voltage [19].

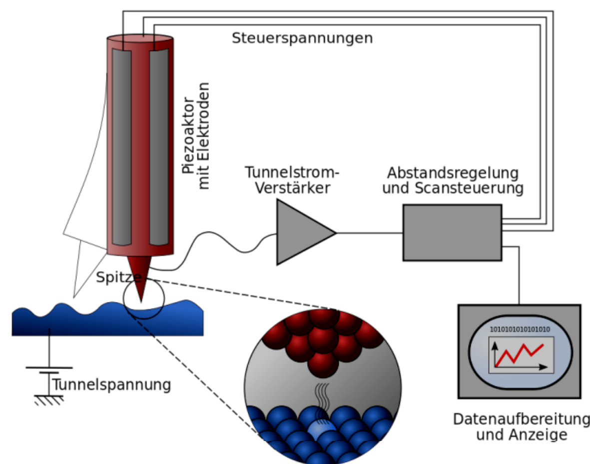

Figure 2.6: *Schematic of scanning tunneling microscopy (STM) [29].*

The basic working principle of STM is based on the one-dimensional quantum mechanical tunnelling of electrons between the tip and surface atom, keeping a tunnel gap distance of few angstroms. STM is using a very sharp metal wire (tip) to scan over the surface of the samples. A constant electrical voltage (bias voltage) is applied between the tip and sample surface. For a very close proximity of the tip and the surface (~Å), the tunneling current between the tip and surface atoms is measured, during the scanning of the tip over a surface. The overlapping of the electronic wave function between tip and surface atoms decreases exponentially with the tunnel gap, which makes the tunnelling

current (~10 pA to 1 nA) very sensitive to the distance between the STM tip and the surface of sample. Topography and surface atomic reconstructions can be achieved, by precisely controlling the relative position of the tip and scanning over the surface. The function of a feedback loop is also important as it maintains a constant tunnelling current during the scanning process of STM [19]. A schematic illustration of the STM is shown in Figure 2.6.

2.3.5 Atomic Force Microscope (AFM)

Surface topography of metal oxide thin films was investigated by atomic force microscopy (AFM). Atomic force microscopy (AFM) was developed when people tried to extend the use of scanning tunneling microscope (STM) technique to investigate the electrically non-conductive materials, like proteins. Scanning tunneling microscope (STM) is use as key components for the invention of number of new scanning probe microscopes (SPM). Out of them, one of the most important is the atomic force microscope (AFM) [26]. AFM is main tools for imaging, measuring the roughness and manipulating matter at the nano-meter range down to atomic scale. AFM consists of a cantilever with a sharp tip/probe (typical radius of curvature at the end for commercial tips is 5-10 nm with rectangular and triangular geometries). The tip/probe of the cantilever (also referred as AFM probe) is located at the free end of a cantilever. The cantilever is made up of silicon or silicon nitride, which makes them very flexible but strong enough to securely hold the tips on their end. The AFM principle is based on cantilever tip assembly, which interacts with the surface atom of the sample. When AFM probe is brought into close proximity of a surface atom, inter atomic forces between them cause the cantilever to bend or deflect. According to Hooke's law force $F = - K \Delta Z$, where K is the spring constant of the cantilever and ΔZ is the deflection. When an AFM probe approaches the surface of sample long range attractive force between the surface and AFM probe causes the cantilever to bend towards the surface. However, as the cantilever moves even closer to the surface, AFM probe contacts the surface and short-range repulsive force starts to dominate. In this situation, repulsive force takes over the force of attraction and causes the cantilever to bend away from the surface of the sample. A laser beam is used to detect cantilever deflections towards or away from the surface. This reflected laser beam is tracked by a position sensitive photo-detector (PSPD) that

picks up the vertical and lateral motion of the AFM probe. The deflection sensitivity of this detector has to be calibrated in terms of how many nanometers of motion correspond to a unit of voltage measured on the detector.

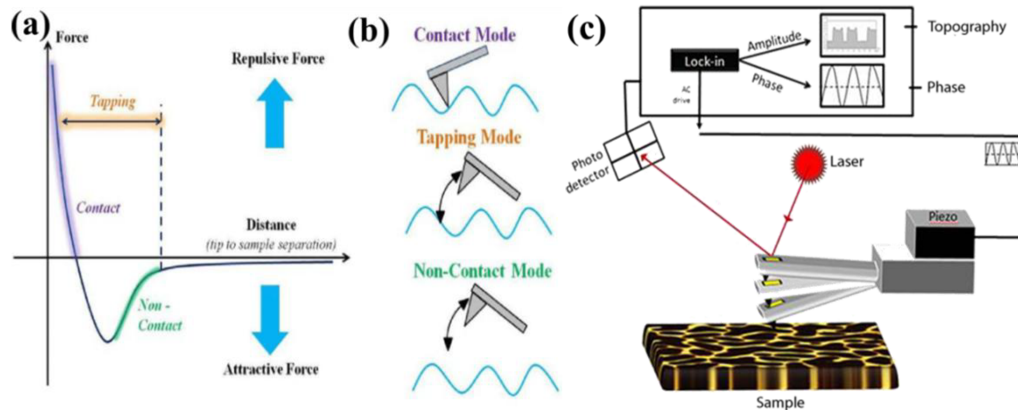

Figure 2.7: *(a) Van der Waals force, (b) imaging modes dependence upon the distance between AFM probe and surface of the sample and (c) schematic diagram of atomic force microscope (AFM) [27].*

A constant height with rough sample exhibits huge risks, causing the damage of the surface of the sample as well as AFM tip. For this reason, mostly a feedback loop is required to adjust the distance between the probe apex and the sample surface atom. Using the feedback loop, a constant force was maintained between the AFM probe and surface atom. Usually, the sample is mounted on a piezoelectric tube, which can move the sample in the 'z' direction for maintaining a constant force. Whereas, x and y directions was used for scanning the surface of the sample. The resultant of the area of the sample represents the topographic map of the sample [5]. The schematic diagram of atomic force microscope (AFM) is shown in Figure 2.7. In addition, AFM is also operated into imaging modes such as contact, non-contact and tapping mode. Figure 2.7(a) and (b) shows schematic diagram of both inter-atomic force between the cantilever and sample and imaging (contact, non-contact and tapping) modes, respectively.

2.3.6 UV-VIS Spectroscopy

The absorption of photon is of a great importance in the fundamental studies of optical properties of the semiconducting metal oxides. UV-visible spectroscopy is used here for the investigation of the optical properties of the oxide materials such as transmission,

absorption, reflection, refraction, and polarization for applications in the field of opto-electrical devices. Such properties are useful to calculate the band gap (direct and indirect), absorption coefficient and refractive index. The equilibrium condition in semiconductor can be described by generation of charge carriers due to absorption of photon. When the photon incident on a material, it may either be reflected, transmitted or absorbed. The absorption phenomena of photon in a material is mostly due to the inner shell electrons, valence band electrons, free charge carriers (including electrons) and some impurity or defects. In an ideal semi-conductor, the valence bands are completely full of electrons at low temperature as they not excited to the higher energy state. Absorption or annihilation of the photon gives the sufficient energy for the excitation of an electron. Hence, electrons can transfer from valence band to conduction band and leaving a hole in the valence band. During this absorption process, however, the energy and momentum conservation must be satisfied.

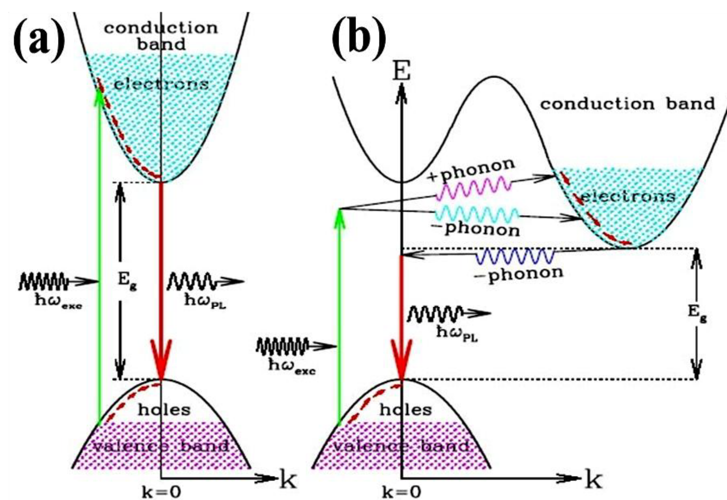

Figure 2.8: *Transitions of electrons from valence to conduction band in (a) direct and (b) indirect band gap [30].*

Basically, two types of optical transitions (band gap) direct and indirect are available for the semiconductors. In the direct band gap, optical transition involves a direct vertical transition of electrons from the valence to the conduction band [shown in Figure 2.8(a)]. If the photon energy is larger than the forbidden gap then direct transition of electrons from the valence to the conduction band are taken place. Both energy and momentum must be conserved during transition in direct band gap of semiconductors. However,

indirect band gap involves simultaneous interaction with lattice vibration. The transitions occurs using two-step process, which is not only involving the photons and electrons but also phonon [shown in Figure 2.8(b)].

The absorption coefficient (α) is a function of photon energy (hv) and given a

$$\alpha = A\frac{(hv - Eg)^n}{hv} \tag{2.10}$$

where, A is a constant (Tauc parameter), hv is the energy of absorbed light, n is the parameter connected with distribution of the density of states [28-29]. The absorption coefficient can be constructed from either the absorption or transmission spectra, using the relation $I = I_o e^{-\alpha t}$. Here, I is the intensity of transmitted light and I_o is the incident light intensity and t is the film thickness. Coefficient $(\alpha hv)^2$ will show a linear dependence on the photon energy (hv) in direct transition. Hence, the plot of $(\alpha hv)^2$ against energy (hv) is expected to be a straight line and the intercept on energy axis at $(\alpha hv)^2$ will give the band gap energy E_g.

2.3.7 Raman Spectroscopy

Raman spectroscopy is a branch of vibrational spectroscopy of molecules [31], based on interaction of electromagnetic radiation with the matter. It is a versatile method, which can be used for both qualitative and quantitative analysis purpose of molecules, crystals and semiconductors [32]. Qualitative analysis has been achieved by measuring the frequency of the scattered radiations, whereas, quantitative analysis has been performed by measuring the intensity of it [33-34]. In Raman spectroscopy, when a monochromatic laser beam (photons) of insufficient energy (to eject the electrons) interacts with the matter scattering process occurs. The frequency of the scattered light, (wave number 50 to 4000 cm^{-1}) directly depends upon the reduced mass of the vibrational unit such as smaller reduced masses give rise to higher frequencies. Basic fundamentals regarding the Raman spectroscopy is also discussed in reference [40].

In principle, when a monochromatic radiation interacts with the matter, it is scattered in all directions. There are two possibilities of scattering called elastic scattering (Rayleigh) and inelastic scattering (Raman). Raman spectra arise due to the inelastic collision between monochromatic incident radiation and the matter. The major part of the scattered light is in

the form of elastic scattering and the energy exchange remains zero during the interaction between incident light and matter. Thus, the Rayleigh scattered radiation has a frequency which is equal to frequency of incident radiation. Only a small fraction of scattered radiation interacts inelastically, known as Raman scattering, where the scattered radiation has a different frequency from the incident radiation. Raman scattering is basically due to the interaction of photons coupled with phonons (molecular vibrations) within the crystal. Interacting photon can lose (stokes scattering) or gain (anti-stocks scattering) energy during the Raman scattering.

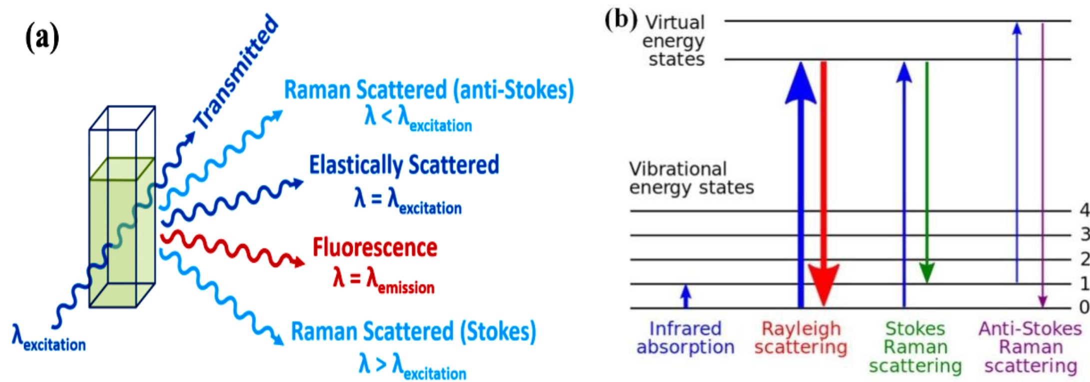

Figure 2.9: *Diagram of energy levels for Rayleigh scattering and Raman scattering with Stokes and Anti Stokes line scattering [35].*

In the Stokes scattering, the frequency of incident radiation is higher than the frequency of scattered radiation as energy is transferred from incident light to the molecules. The excited molecules from the virtual state come back to its vibrational state rather than its ground state and a lower energy of photon is emitted. On the other hand, the anti-Stokes lines appear in Raman spectrum when the frequency of incident radiation is lower than the scattered radiation. Here, the molecules were already in its excited vibrational state, due to prior excitation or thermal disturbance. These molecules are now excited to a virtual state and emitting a higher energy photon during their return to the ground state as energy is transferred from the molecules to the incident light. However, Stokes bands are more intense than anti-Stokes bands and are measured in conventional Raman spectroscopy. While anti-Stokes bands are measured with fluorescing samples because fluorescence causes interference with Stokes bands [19]. Figure 2.9 displays a basic diagram of energy levels for Rayleigh and Raman (Stokes and Anti Stokes) scattering. Raman scattering strongly depends upon the wavelength of incident radiation

(optical components) and the spectra represents as an intensity vs wavelength shift, recorded in the range of 4000 -10 cm^{-1}.

2.3.8 X-Ray Photoelectron Spectroscopy (XPS)

X-ray photoelectron spectroscopy (XPS) is a non-destructive technique for qualitative and quantitative chemical analysis of the samples surface. It is an extremely surface sensitive method for the detection of elemental analysis, atomic composition, mutual bonding and charge transfer as well as chemical oxidation states of any material. However, XPS is very much surface sensitive and provide the information only up to a depth of few nm, as the escape depth of the photoelectron in very much limited. The fundamental theory related to XPS [36, 37] is introduced in the following.

Photoelectron Spectroscopy is based on the principal of photoelectric effect, where the electrons are emitted using X-rays as a photon source. When a sample surface is irradiated by a characteristic X-ray, several core level photoelectrons are emitted from the surface of sample along with secondary and auger electrons. After absorbing the X-ray photon of energy hυ, the core level electrons is able to overcome their binding energy (E_b) and emit from the surface with a certain kinetic energy (E_k), shown in Figure 2.10(a).

To understand the phenomena of XPS, excitation of a carbon 1s (core level) electron with X-ray photons can be considered. Upon absorption of X-ray, the photon energy will be transferred to the carbon 1s electron. Part of this energy is used to overcome the binding energy of carbon 1s electron and become free. The excess energy of the photon will contribute as kinetic energy of the associated photo-electron, which is leaving the material surface. In 1914, Rutherford explains the relation between the kinetic energy of the electrons with excitation energy and binding energy [37]. Therefore, the kinetic energy of the core level electron can be described as

$$E_k = h\nu - E_b - \phi \quad (2.11)$$

where, $h\nu$ is the energy of the X-ray photon, E_k is the kinetic energy of the emitted electron and ϕ is the work function of the analyzer.

In present work, two different X-ray sources such as $Mg\ K_\alpha$ (1253.6 eV) and $Al\ K_\alpha$ (1486.6 eV) lines are used for XPS studies. Both sources are having relatively high energy and narrow width. Although, X-rays can penetrate up to few mm into the material, however, XPS can only sense up to ~10 nm of depths. Escape depth of the photo-electrons are mainly limited due to inelastic scattering within the material as shown in Figure 1.10(b) and the effect of inelastic scattering is described by the Beer-Lambert law [18].

$$I_z = I_0 \exp\left(-\frac{z}{\lambda \sin\theta}\right) \tag{2.12}$$

where, I_z is the intensity of photoelectrons (nA) at a depth z (nm) and I_0 is the intensity from the surface atoms (nA), λ is the inelastic mean free path (nm) and θ is take off angle of photoelectrons [37]. Escape depth λ is defined as the distance normal to the surface at which the possibility of an electron escaping without any significant energy loss due to inelastic scattering process dropped to 36.8% of its original value. Hence, the detector can only measure the photoelectron current from a layer of atoms up to certain depth as the deeper level photoelectrons are attenuated by the thickness of the material. Sampling depth is from which 95% of the photoelectrons originate and is equal to about three times the escape depth. Commonly, escape and sampling depths are calculated by following equations as "Escape depth z = $\lambda\ sin\theta$" and "Sampling depth = $3\lambda\ sin\theta$", where λ is the inelastic mean free path (nm) and θ is electron take off angle.

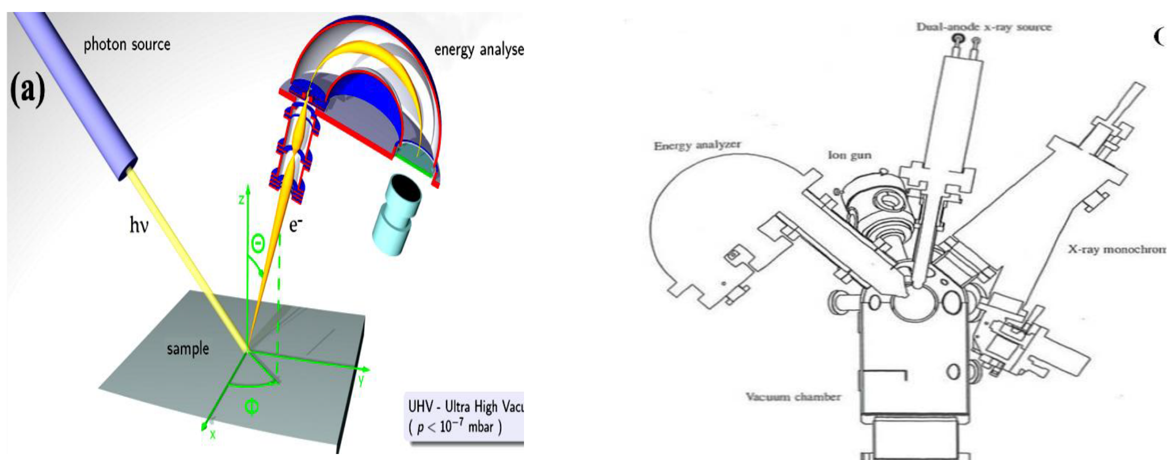

Figure 2.10: *(a) Photoemission process of electrons [38] and (b) schematic image of X-ray Photoelectron Spectroscopy (XPS) [36].*

Typically, two types of XPS spectra such as survey and elemental spectra are obtained. A survey spectrum is given the overall information about the elements present in the sample. The maximum survey spectra range depends on the X-ray sources, ($Mg\ K_{\alpha}$ or $Al\ K_{\alpha}$) and is given by the excitation energy minus the work function as the binding energy of the photoelectrons cannot exceed the excitation energy of the X-ray photons. Elemental spectra are obtained with smaller step size and pass energy with higher resolution. Therefore, high resolution scan of any element, which is present in survey scan, can be obtained by elementary spectra to determine atomic composition analysis with higher accuracy [36]. In addition, relative comparisons can also be done from the areas under the curves in XPS spectra.

2.3.9 Four Probe Resistivity Measurements

Four probe electrical characterizations techniques are used for the measurement of various electrical properties of metal oxide thin films such as resistivity (ρ), carrier concentration, carrier mobility, hall coefficients etc. Electrical resistivity is a key physical property of materials to check the electronic performance of any semiconductor devices. Apart from quantum confinement scale, electrical resistivity is a fundamental material's property, does not depend on the shape of the sample. Therefore, it is necessary to measure the accurate value of ρ of a given materials. Within a perfect crystal, in principle, the velocity of free electrons should continuously increase with time in presence of an applied electric field. But in practical, the velocity reaches a saturation value called the drift velocity, which suggests that some dragging force named resistance must be present originated from the real crystal imperfections such as defects, dislocations, grain boundaries and lattice thermal vibrations. Apart from the material's resistivity, another important technical factor called contact resistance can play a very important role in any kind of sensitive electrical measurements. Different techniques are used to decouple the contact resistance/resistivity contribution for the electrical measurement such as collinear probe method and Van der Pauw method (Hall Effect). However, four probe resistivity measurement techniques can effectively exclude the contact resistance (R_c) and spreading resistance (R_{sp}) resistances of any conducting films. Mainly, two major approaches, collinear four probe and Van der Pauw are used for

determining the resistivity of semiconducting metal oxide thin films. The collinear four-point probe method is applicable when the probes distance is much smaller as compared to the dimension of the film surface and the probes are far away from the edge of the sample. The arrangement of a four-point probes method is shown in Figure 2.11. Four equally spaced probes are placed at the center of oxide thin film and brought in contact using conductive silver ink. A constant current is passed through the outer two probes and the potential drop across the inner two probes is sensed. The resistivity (ρ) of the film is calculated using the formula

$$\rho = \left(\frac{v}{I}\right)\left(\frac{w \times t}{1}\right) \tag{2.13}$$

where, V is voltage drop across two faces (volts), I is the current passes through it (ampere), w is the width of thin film (cm), t is the thickness of thin film (cm) and l is the length of the sample (cm). If the sample shape is considered as a square, then w = l and the sheet resistance (ρ_{sh}) is given as

$$\rho_{sh} = (V / I) \times CF \tag{2.14}$$

where, CF is correction factor that depends on the probe configuration and sample geometry [48]. If probe spacing (s) is very small as compared to the width (d) of a sample (d<<s) then the CF for thin films (t<<s) is equals to CF = [$\pi/ln(2)$], while it is found to be CF = (2πs) for thick films (t>s). More details related to the correction factors for different geometrical shapes were discussed by *Haldor Topsoe* [40].

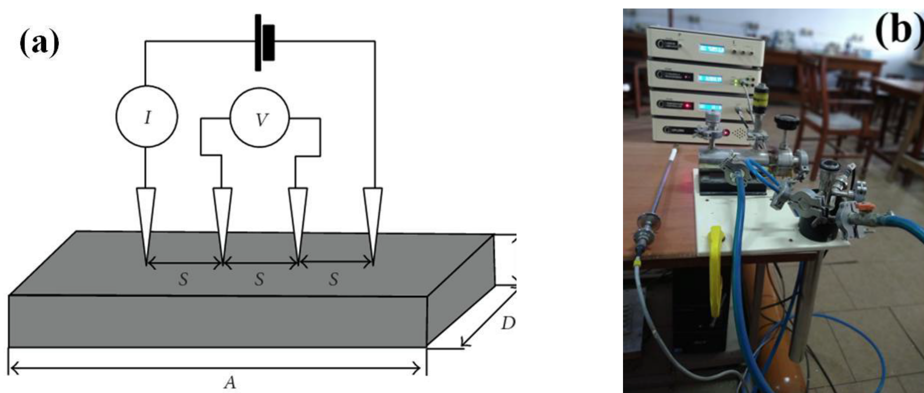

Figure 2.11: *(a) A schematic diagram of (a) four point probe [39] (b) setup image of four probe resistivity measurements.*

In our case, four probe resistivity measurement setup [shown in Figure 2.11] consists of a doubled walled hollow dewar, known as cryostat. The sample is mounted on the sample holder and loaded inside a cryostat using long non-magnetic steel rod. Silicon diode is used to measure the sample temperature (uncertainty < 1°C), which is connected to the sample holder. The position of the Si diode is very close to the sample to avoid any lag in temperature readout. The temperature can be varied from *RT* to 450 K during the *I-V* and the *R-T* measurements. To measure the ρ at certain temperature, proportional–integral–derivative (PID) temperature-controlled arrangement is used to heat the sample in a controlled manner. Silver epoxy/paste and copper wire contact are used to ensure a good electrical contact. R-T measurements with heating and cooling cycle have been performed on metallic thin films in air as well as under helium ambient inside a close cryostat. In addition, to minimize any kind of contact errors, all I-V data was recorded at a particular temperature with heating cooling cycles and the corresponding slope (related to the thermal coefficient of resistivity) was used to measure the R-T plot.

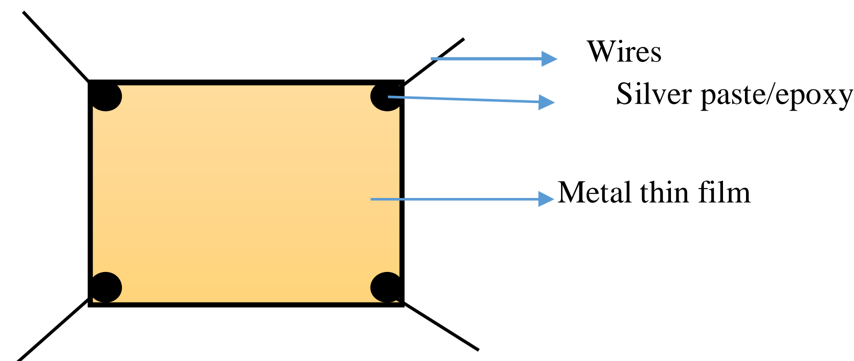

Figure 2.12: *(a) A schematic diagram of four point of Van der Pauw method for rectangular geometric.*

Van der Pauw method is a useful technique for the accurate measurements of resistivity and Hall coefficient of samples having any of any arbitrary shape. In our case it is used to determining the resistivity, carrier concentration, mobility and hall coefficient of metal oxides thin films. In this method, the sample thickness must be less than the width and length of the sample. To measure the resistivity and Hall coefficient of the samples, four contacts (ohmic) must be placed at the corner (boundary / perimeter) of the sample [Figure 2.12]. All the contacts should be constructed from the same bunch

of wire as well as four contacts on sample should be of the same material, to minimize thermoelectric effects.

The electrical resistivity of a semiconductor thin film can be written using the Ohm's law $[\rho = 1/(ne\mu)]$, where 'ρ' is resistivity of thin film; e is the charge of an electron, n is the carrier concentration and μ is the carrier mobility. According to Ohm's law, carrier mobility affects the resistivity of thin film where a low resistivity can be achieved by increasing the carrier concentration and its mobility. At some point, increase in charge carriers density will decreases the mobility of thin film due to the mutual scattering. Hence there is an optimization relation between the charge carrier density and mobility for achieving the lowest resistivity. In the present work, single oxide phase of ZnO and CuO thin films are used for the measurements of the resistivity (ρ), carrier concentration (n), carrier mobility (μ) and sheet resistance, using the Vander Pauw configuration. The ohmic contacts were made using silver paste, which was symmetrically applied at the corners of the thin film. Consider that R_1 be the potential difference between A and B points per unit current through C and D or vice versa. Similarly, R_2 is the potential difference between B and C points per unit current through D and A. Then sheet resistance (R_{sh}) can be calculated using the relation [41]:

$$R_{sh} = \left(\frac{\pi}{\ln 2}\right)\left(\frac{R1 + R2}{2}\right) f\left(\frac{R1}{R2}\right) \tag{2.15}$$

where $f\left(\frac{R1}{R2}\right) = 1 - 0.3466\left(\frac{R1 - R2}{R1 + R2}\right)^2$ is the *Van der Pauw* function.

The Hall signal was measured between two ends while passing the current through the other two ends and the mobility is given as:

$$\mu = \Delta R \times \frac{10^8}{BR_{sh}} \tag{2.16}$$

where, ΔR is the change in resistance due to magnetic field (B), which is applied to measure the Hall voltage. Carrier concentration is calculated by the equation:

$$R_H = \mu\rho. = 1/ne \tag{2.17}$$

The type of carriers can be explained from the sign of the R_H. The negative values of R_H correspond to the electrons (n-type) and positive values to holes (p-type) responsible for conduction.

2.3.10 Gas Sensor Set-Up

To investigate the chemi-resistive response of metal oxide nanostructures, during exposure to an oxidized/reducing gas/vapour, a home build gas sensing set-up is used to measure the variation of surface resistance of the thin oxide film. The gas sensing unit consists of an airtight glass vacuum chamber of diameter 30 cm and of height 50 cm. The SMO thin film used as a sensing material surface was kept over a heater, inside the vacuum chamber connected with an inlet and an outlet port for gas transportation. The inlet is connected to multi-component gas mixer, which controls the gasses flow rate at ppm level. The dry air and the target gas enter into the gas mixer separately and then mixed as per the requirement by a computerized technique. The vacuum chamber temperature controller is based on the PID control scheme, which automatically adjusts the variation in reaction chamber temperature around a fixed value (operating temperature). Au contact electrodes wires are connected to a digital multi-meter (Keithley) to measure the variation in resentence in presence of a target gas (CO). The computer programming is performed in multi-component gas mixer, which can control the flow of pure dry air and target gas for particular time period. Figure 2.13 shows schematic view of gas sensing measurement system and (b) digital image of measurement setup and vacuum chamber.

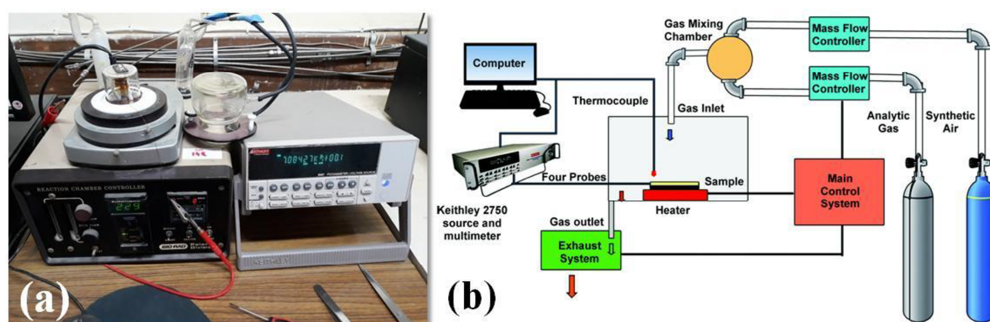

Figure 2.13: *Schematic view gas sensing measurement system and (b) digital image of measurement setup and vacuum chamber [42].*

MOS thin a film deposited on an insulting substrate (glass or silicon) is used as a sensing material for CO gas. Prior to any sensing experiment, a thin gold film of ~100 nm was deposited on it using a finger mask. These Au contacts are used as the top (ohmic) electrodes of the SMO thin film sensor. A Cu metal mask is developed (for the

Au deposition), by a controlled chemical etching process using $FeCl_2$ solution. Schematic top and side views of metal oxide layer with Au electrode are show in Figure 2.14 (a, top view). Gas sensing platform with a thin film metal oxides gas sensor the kept over a base heater and is shown if Figure 2.14(b).

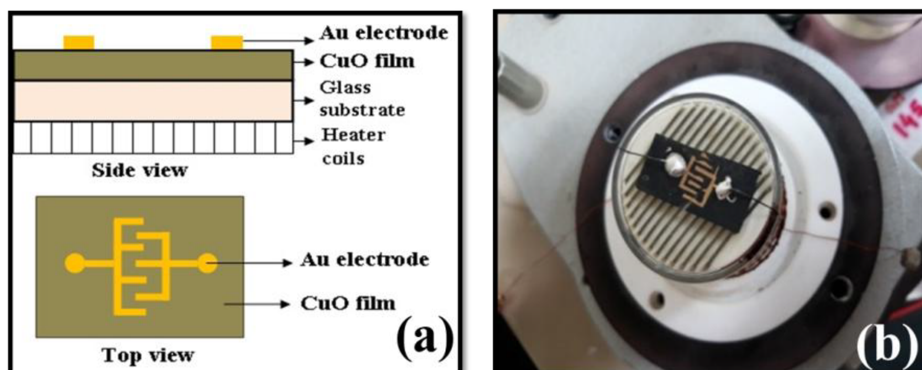

Figure 2.14: *Schematic side and top views, (b) digital image of metal oxide thin film gas sensor with top Au contacts.*

Within this work, dry air (300 CCM) was continuously flown into the airtight glass chamber during the measurement. The CO gas concentrations were controlled by changing the mixing ratio of dry air to CO gas, using a mass flow controller (series 2000, computerized multi-component gas mixer). The operating temperature for MOS based gas sensors was controlled and monitored using a PID temperature micro-controller. MOS thin films were pre-heated for overnight to improve the thermal stability of the contact junction. The whole device was setup in such a way that data recording and monitoring were automatically performed. Apart from CO sensing, a static mode of ethanol vapour sensing has also been performed. Initially, low pressure of ~650 mmHg was created in a closed glass chamber and increased qualitatively with time (maximum 90 min). In this case, device impedance was measure using a GWInstek 6300 LCR meter at room temperatures.

2.3.11 Photo- catalytic Process

The photo catalytic degradation of Dyes (Methylene Blue) using catalyst under visible light is performed at room temperature (RT). Within this work, the dye solution of methylene blue (MB) of 2×10^{-4} M concentration is prepared by dissolving it in 2ml of

Hydrogen Hydrate (HH) with DI water prior to any degradation process. The photo catalyst is introduced into the dye solution and is exposed to visible light for different time periods. A tungsten lamp is used as the visible light source. It is known that MB is relatively stable in aqueous solutions upon solar irradiation. A photo-degradation reaction is performed when the whole reaction is maintained in darkness apart from the visible light used. The dark blue color of MB dye solution is gradually lightened during the photo-degradation process and after certain time of period, the MB dye solution become colorless. The degradation kinetics of Dyes is estimated by a UV-visible spectroscopy. The UV-Vis spectrum was recorded after every interval of cycle under visible light irradiation for various time periods at a constant concentration (2×10^{-4} M) of dye solution. From the recorded spectra, percentage of dye removal is calculated using the standard formula:

$$D = \frac{(A_o - A)}{A_o} \times 100\%$$

where, A_0 is the initial concentration of MB and A is the concentration of MB after irradiation of the samples in desired time interval. The degree of absorbance of the samples was measured by the UV-vis spectrophotometer described in experimental section of Chapter 3.

Bibliography

[1] M. Ohring, “Materials Science of Thin Films”, 2nd Edition Academic Press, New York (2002).

[2] L. Holland, “Vacuum Deposition of Thin Films”, University of Michigan, Wiley (1966) 541

[3] P. Martin, “Deposition Technology: Thermal Evaporation” (2012).

[4] K. Wasa, M. Kitabatake and H. Adachi, “Thin Films Material Technology: Sputtering of Compound Materials”, William Andrew Publication, Springer (2004).

[5] E. A. Davies and N. F. Mott, Philosophical Magazine 22 (1970) 0903.

[6] F. K. Mugwanga, P. K. Karimi, W. K. Njoroge, O. Omayio and S. M. Waita , International Journal of Thin Film Science & Technology 2 (2013) 15.

[7] H. Zhu, J. Zhang, C. Li, F. Pan, T. Wang and B. Huang, Thin Solid Films 517 (2009) 5700.

[8] https://www.adnano-tek.com/magnetron-sputtering-deposition-msd.html

[9] https://www.dentonvacuum.com/products-technologies/magnetron-sputtering/

[10] K. Kusaka, D. Taniguchi, T. Hanabusa and K. Tominaga, Vacuum 66 (2002) 441.

[11] F. Medjani, R. Sanjines, G. Allidi and A. Karimi, Thin Solid Films 515 (2006) 260.

[12] Harold P. Klug and Leroy E. Alexander, “X-Ray Diffraction Procedured: For Polycrystalline and Amorphous Materials” 2nd Edition, University of California, A Wiley-interscience publication (1974).

[13] C. J. Humphreys, Acta Crystallography A69 (2013) 45.

[14] N. Sadananda Kumar, K. V. Bangera and G. K. Sivakumar, Applied Nanoscience 4 (2014) 209.

[15] Y. Zhao and J. Zhang, Journal of Applied Crystallography 41, (2008) 1095.

[16] P. E. J. Flewit and R. K. Wild, “Physical methods for material characterization” 2nd Edition, IOP publishing, London (2003).

[17] A. H. M. Areef Billah, “Investigation of multiferroic and photocatalytic properties of Li doped BiFeO3 nanoparticles prepared by ultrasonication” Bangladesh University of Engineering and Technology, Dhaka, Bangladesh (2016).

[18] F. Y. Zhu, Q. Q. Wang, X. S. Zhang, W. Hu, X. Zhao and H. X. Zhang, Nanotechnology 25 (2014) 18.

[19] S. Gangopadhyay, “Growth, Surface Structure and Morphology of Semiconductor Nano-Structures”, Institute of Solid State Physics, University of Bremen (2006).

[20] R. F. Egerton, "Physical principle of electron microscopy: an introduction to TEM, SEM and AFM" Springer (2005).

[21] https://www.globalsino.com/EM/page1985.html

[22] http://www.hk-phy.org/atomic_world/tem/tem02_e.html

[23] J. A. Kubby and J. J. Boland, Surface Science Report 26 (1996) 61.

[24] R. Wiesendanger, "Scanning Probe Microscopy and Spectroscopy, Methods and Applications" Cambridge University Press, Cambridge (1994).

[25] https://en.wikipedia.org/wiki/Scanning_tunneling_microscope.

[26] F. Micheltti and P. Mark, Journal of Applied Physics Letter 10 (1967) 136.

[27] M. Paul Narchi, Physique, Universite Paris-Saclay (2016).

[28] F.A. Settle, "Handbook of instrumental techniques for analytical chemistry" Prentice, New Jersey (1997).

[29] J.M. Chalmers, H.G.M. Edwards and M.D. Hargreaves, "Infrared and Raman spectroscopy in forensic science" 1st Edition, John Wiley & Sons, United Kingdom (2012).

[30] A. Li, ASP Conference Series, 000, (2003)

[31] J.M. Chalmers, H.G.M. Edwards and M.D. Hargreaves, "Infrared and Raman spectroscopy in forensic science" 1st Edition, John Wiley & Sons, United Kingdom (2012).

[32] D. A. Skoog, F. J. Holler and S. R. Crouch, "Principles of instrumental analysis" 6th Edition, Cengage Learning (2006).

[33] H. H. Willard, L. L. Meritt Jr., J. J. Deann and F. A. Settle Jr., "Instrumental methods of analysis" 7th Edition, CBS Publisher & Distributors, New Delhi (1988).

[34] M. Panich, A. I. Shames and T. Nakajima, Journal of Physics and Chemistry of Solids 62 (2001) 959.

[35] https://en.wikipedia.org/wiki/Raman_spectroscopy

[36] J. F. Moulder, W. F. Stickle, P. E. Sobol and K. D. Bomben, "Handbook of X-ray Photoelectron Spectroscopy" Physical Electronics Division 190 (1979).

[37] J. F. Watts and J. Wolestenholme, "An Introduction to Surface Analysis by XPS and AES" John Wiley & sons, England (2003).

[38] Photoelectron spectroscopy, khan academy

[39] S. Ummartyotin, J. Juntaro, C. Wu, M. Sain and H. Manuspiya, Journal of Nanomaterials, 606714 (2011) 7.

[40] H. Topsoe, "Semiconductor Division" 2nd revised Edition, "Geometric factors in four point resistivity measurements", Bulletin No. 472-13 (1968).

[41] I. J. van der Pauw, Philips Research Report 13 (1958) 1.

[42] K. Sankarasubramanian, P. Soundarrajan, T. Logu, K. Sethuraman and K. Ramamurthi, New journal of Chemistry, 2 (2018) 10.